# Mm-Wave Cavity-Backed Multi-Linear Polarization Reconfigurable Antenna

Shu-Lin Chen, *Member, IEEE,* Yanhui Liu, *Senior Member, IEEE,* He Zhu, *Member, IEEE,* Dingzhao Chen, and Y. Jay Guo, *Fellow, IEEE*

***Abstract*—Polarization reconfigurable antennas at millimeter-wave (mm-wave) frequencies are important technologies for 5G and beyond wireless communications systems. This paper presents a mm-wave multi-linear polarization (LP) reconfigurable antenna. It employs a resonant $TM_{510}$-mode air-filled cavity as the base, and a circular array of slots is uniformly etched on its top surface to provide a rotationally-symmetrical "excitation" for the multi-LP antenna. An upper substrate printed with engineered patch layers is introduced above the slots for an in-phase high-gain composition, and it is mechanically rotated to facilitate the multi-LP reconfiguration. Each slot radiation is separately monitored and analyzed by using single-slot cavity models. A final multi-LP antenna that can switch among five LP states at mm-wave band was constructed. To overcome the classic high sidelobe problem associated with circular arrays, a modified bottom layer is introduced to the multi-LP antenna. The measured overlapped bandwidth of the optimized multi-LP antenna ranges from 28.58 to 28.99 GHz. For all of the five LP states, the simulated and measured sidelobe levels are $-13$ and $-10$ dB, respectively. The measured realized gains are varied from 15.5 to 16.8 dBi in the overlapped operating bandwidth. This is the first time to report a mm-wave multi-LP reconfigurable antenna.**

***Index Terms*—Cavity-backed antenna, millimeter-wave (mm-wave), multi-linear polarization (LP), polarization reconfigurable antenna, resonant cavity**

## I. Introduction

RECONFIGURABLE antennas can alter their characteristics according to the varying environments [1]–[7]. They have emerged as an important technology that can significantly improve the overall system performance such as communications data rates and range. Polarization reconfigurable antennas are particularly attractive for applications that require polarization flexibility and minimum polarization mismatch [8]–[13].

Considerable efforts have been devoted to advancing the development of polarization reconfigurable antennas. Three main types of polarization switching schemes have been reported in the open literature, including switching between two circular-polarization (CP) states [14]–[16]; CP and linear-polarization (LP) states [17]–[20]; multiple-LP (multi-LP) states [21]–[25]. Multi-LP antennas generally have a number of switchable LPs with an equal angle interval ($\Delta\phi$), and the LPs number $P = 180^\circ/\Delta\phi \geq 4$. This multi-LP functionality can deliver many benefits in practical systems, for example, minimizing the polarization mismatch for the randomly linearly-polarized incoming waves in body-centric wireless communication systems [23]. To facilitate the multi-LP reconfiguration, the researchers utilized innovative switching techniques in either feed networks [21], [22] or main radiators [23]–[25]. A 45°-interval four-LP reconfiguration was achieved in [21] and [22] that respectively employed switchable shorting vias and feed probes for a circular patch antenna. By controlling PIN diodes soldered on the radiating arms of multiple dipoles, a number of LP states was obtained in [23]–[25].

Note that all of the previously reported multi-LP reconfigurable antennas are operating at lower-frequency bands, i.e., less than 5 GHz. Currently, mm-wave antennas have drawn special attentions for 5G and beyond wireless communications [26]–[28]. They can facilitate a very high-speed data communication link with a much compact configuration. Several interesting polarization-reconfigurable antennas have been reported to operate at mm-wave band. A dual-CP reconfigurable antenna was developed in [29] that can operate from 27.2 to 28.35 GHz by switching two pairs of PIN diodes. A mechanical rotation of the reflective panel of a reflectarray antenna was presented in [30] to achieve the polarization switching among LP, RHCP, and LHCP. Nevertheless, none of the above mm-wave antennas could provide a multi-LP reconfigurable functionality.

To the best of the authors' knowledge, it has never been reported to achieve a mm-wave multi-LP reconfigurable antenna. One may opt to scale up the operating frequency of those low-frequency multi-LP antennas presented in [21]–[25] to the mm-wave band. However, several challenges prevent this choice. First, since antenna wavelength would be much smaller at mm-wave band, it is difficult to integrate main radiators, feed network, and PIN diodes along with their biasing circuits into such a compact configuration. Furthermore, these PIN diodes and biasing circuits will have a bigger impact on antenna's radiation performance. Finally, few PIN diodes are found to operate well at mm-wave band, and they usually introduce large losses. In this paper, a mm-wave multi-LP $TM_{510}$-mode cavity antenna is presented to switch among five LP states by a mechanical rotation of its upper copper-cladded substrate. A complete process of antenna design, analysis, and measurement is provided. The measured realized gains

Manuscript received XXX. This work was supported by the Australian Research Council (ARC) Discovery Project (DP) 160102219 grant. *(Corresponding author: Yanhui Liu)*

S.-L. Chen, H. Zhu, and Y. J. Guo are with the Global Big Data Technologies Centre (GBDTC), University of Technology Sydney (UTS), Ultimo, NSW 2007, Australia. (E-mail: shulin.chen@uts.edu.au)

Y. Liu is with the Yangtze Delta Region Institute (Quzhou), University of Electronic Science and Technology of China (UESTC), Quzhou, Zhejiang 324000, China. (E-mail: yhliu@uestc.edu.cn)

D. Chen is with the Institute of Electromagnetics and Acoustics, Xiamen University, Fujian 361005, China.

vary from 15.5 to 16.8 dBi for the five LP states of the final fabricated prototype in the operating bandwidth.

The main contributions of the paper can be summarized as follows. First, to address the challenge of realizing mechanically-reconfigurable multi-LPs, a rotationally-symmetrical base "excitation" technique is developed. The base "excitation" is accomplished by a $TM_{510}$-mode cavity etched with a circular array of rectangular slots. This way the multi-LP reconfiguration is simplified to achieve a single high-gain low-cross-polarization LP state. Second, to align polarization direction and adjust phase values of the E-fields radiated from these rotationlly-etched slots, single-slot cavity models are presented to analyze and monitor radiating behaviors of each slot separately. It facilitates the design and optimization of the patch surfaces printed on the upper substrate for each slot's radiation adjustment. Third, the five LPs are attained and reconfigured by rotating the upper substrate. This reconfiguration avoids rotation of the antenna's feed and, hence, makes the presented multi-LP system more feasible in practical applications. Furthermore, the radiation patterns and realized gains are almost invariant for all the five LP states. Fourth, to overcome the classic high sidelobe problem associated with circular arrays, a simple method that uses a modified bottom layer is introduced to the multi-LP antenna.

## II. Circular Cavity and Polarization Reconfiguration

Circular cavities can have rotationally symmetrical field distributions. A $TM_{510}$ resonant mode can be excited in a circular air-filled cavity. In this work, we chose $TM_{510}$-mode cavity as a tradeoff among antenna gain, complexity, and bandwidth. Needless to say, the configuration can be easily extended to cavities of different modes. A mechanically-rotatable copper-cladded substrate is introduced above the cavity for polarization reconfiguration. Operating mechanism of the multi-LP antenna is presented.

### A. Resonant Mode Excitation

A circular air-filled cavity excited with a rectangular waveguide is considered as the base configuration. Its side and top views are shown in Fig. 1 (a) and (b), respectively. The circular cavity has a radius of $R_c$ and a height of $h_c$. It has three walls, i.e., a top wall, a bottom wall, and a peripheral wall. All of the walls are assumed with PEC boundaries in the initial study.

A standard WR-28 rectangular waveguide is employed as a feed to excite the cavity's resonant mode. Its recommended operating frequency ranges from 26.5 to 40 GHz. One notices from Fig. 1 (b) that the waveguide's long side is placed along $y$-axis, and its short side is aligned with $x$-axis. Its center point has an offset distance of $x_w$ along $x$-axis with respect to the cavity's center.

This waveguide-excited air-filled cavity was simulated by using the full-wave simulator ANSYS HFSS. Optimized values (in millimeters) of those parameters are: $h_c = 3$, $R_c = 14.5$, and $x_w = 6.5$. Fig. 2 shows top view of E-field magnitudes excited in the air-filled cavity at 29.25 GHz. One

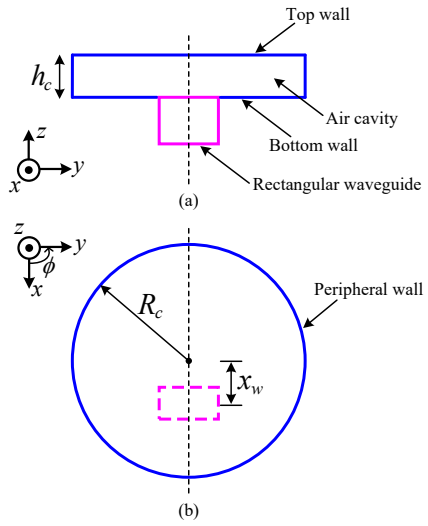


Fig. 1. Configuration of the waveguide-excited air-filled cavity. (a) Side view. (b) Top view.

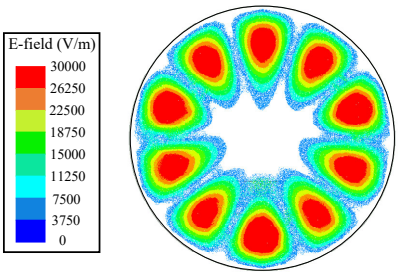


Fig. 2. Top view of E-field magnitudes excited in the air-filled cavity at 29.25 GHz.

observes that a $TM_{510}$ resonant mode is produced in the cavity, i.e., there are ten half-wavelength sections distributed along the azimuthal direction. Each half-wavelength subsection is almost identical and, hence, the cavity along with this $TM_{510}$-mode distribution can be regarded to have a rotational symmetry along the azimuthal direction. The angle $\Delta\phi_0$ of this rotational symmetry is obtained as $\Delta\phi_0 = 360°/10 = 36°$. It should be pointed out that E fields are out-of-phase in any two adjacent half-wavelengths due to the inherent property of the resonant mode.

### B. Multi-Linear Polarization Reconfigurable Mechanism

While one could etch slots on top of the resonant cavity for far-field radiations, only a fixed polarization state is achievable. In order to attain the desired reconfigurable multiple LPs, one has to incorporate a switching freedom into the slotted resonant cavity. Since the resonant cavity along with its feeding cables could not be rotated in many practical applications, an upper copper-cladded substrate is introduced and located above the slotted cavity. The basic idea is to facilitate the multi-LP reconfiguration by mechanically rotating the upper substrate. A subsequent mechanically reconfigurable multi-LP antenna is proposed, and its schematic side view is shown in Fig. 3.

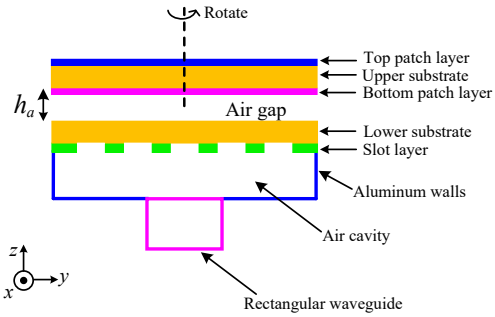


Fig. 3. Schematic side view of the mechanically reconfigurable multi-LP antenna.

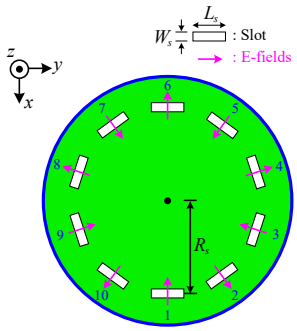


Fig. 4. Top view of the slot layer etched with ten slots. The tangential E-fields induced on each slot are illustrated at an instant time.

In realization of the air-filled cavity, material of the bottom and peripheral walls is chosen as Aluminum, and the top wall is replaced by a lower substrate printed with a metallic slot layer on its bottom. Top metal on the lower substrate is completely removed. A mechanical-rotatable substrate, i.e., the upper substrate, is located above the lower substrate with an air gap of $h_a$. This air gap is preserved to ease mechanical rotation of the upper substrate. Top and bottom patch layers are, respectively, printed on top and bottom layers of the upper substrate. Both the upper and lower substrates are RT/Duroid 5880 with a dielectric constant of 2.2, a loss tangent of 0.0009, and a height of 0.508 mm.

On the slot layer, a circular array of ten slots is uniformly etched on the slot layer as shown in Fig. 4. The center point of each slot sits on the circle with a radius of $R_s$. All slots have a length of $L_s$ and a width of $W_s$. Furthermore, each slot is centrally located on top of one corresponding half-wavelength subsection. The slotted cavity is then rotationally symmetrical with an angle $\Delta\phi_0$, where $\Delta\phi_0 = 180/5 = 36°$. Obviously, it provides a symmetrically-rotatable "excitation" for the upper copper-cladded substrate. Assume the antenna's co-polarization (co-pol.) E-fields are directed along $\phi = \alpha_0$ plane at the broadside direction when the upper substrate is initially fixed. After it is rotated with an angle of $\Delta\phi_0$, the antenna's co-pol. E-fields will be along $\phi = \alpha_0 + \Delta\phi_0$ plane owing to the symmetrical "excitation". In total, when the rotation angle of the upper substrate increases from 0 to $4\Delta\phi_0$ with an interval of $\Delta\phi_0$, five reconfigurable LP states will be obtained. One may conclude that the five-LP reconfiguration is then simplified to achieve a high-gain low cross-polarization (x-pol.) LP state when the upper substrate is initially fixed.

It is common knowledge that co-pol. E-fields radiated from a rectangular slot are oriented in parallel with the narrow side of the slot. Given the rotational distribution of these slots etched on the slot layer, the co-pol. E-fields radiated from each slot will have different polarization angles at the broadside. Furthermore, due to the out-of-phase E-fileds excited in any two adjacent half-wavelengths, the co-pol. E-fields radiated from two adjacent slots will also have 180° phase difference. As an illustration, Fig. 4 depicts a schematic view of tangential E-fields induced on each slot at an instant time. The composite far-field radiation of the ten slots will inevitably have a low gain with a high x-pol. level. It thus requires a careful design of the metallic patch layers printed on the upper substrate to adjust the fields radiated from each slot.

To facilitate the above investigation, each slot radiation will be separately monitored and analyzed with a single-slot cavity model. One finds from Fig. 4 that the induced E-fields for the slots numbered with $N$ ($1 \leq N \leq 5$) and $N+5$ are almost the same. Take Slot 1 and Slot 6 as an example. They are oriented in opposite directions along $x$-axis with respect to the center of their corresponding half-wavelength subsections. This opposite orientation compensates for the out-of-phase E-fields within the two corresponding subsections and, hence, leads to the almost same induced E-fields on Slot 1 and 6. Subsequently, one only needs to analyze half of the ten slots, e.g., Slot 1 to 5, for achieving the desired high-gain low-x-pol. radiation. Five single-slot antenna models that respectively etch Slot 1 to 5 are simulated for this analysis. Detailed investigations are given in the following section.

## III. Single-Slot Cavity Antenna

The basic configuration of the single-slot antenna models is the same as shown in Fig. 3. In each model, only the etched slot as well as the patch layers printed on the upper substrate is varied. The patch layers are centrally located above the slot for radiation adjustment. The initially-fixed reference $\phi = \alpha_0$ state can be selected based on custom-designed requirement. In this work, $\alpha_0$ is chosen as 36°. It is obvious that co-pol. E-fields radiated from Slot 2 have the same polarization with the reference one and, hence, one has to alter the polarization direction of E-fields radiated from other four slots. As aforementioned, one should also optimize far-field phase value of each slot radiation for an in-phase composition. Note that the far-field phase value in each model is obtained with the same global coordinate system in ANSYS HFSS.

### A. Study on Slot 1 and 3

Compared with the reference polarization along $\phi = 36°$ at the broadside, the co-pol. E-fields radiated from Slot 1 (or Slot 3) have a 36° polarization angle difference. This difference can be mitigated by employing a closely-spaced rectangular patch. Take the case when only Slot 1 is etched as an example. Fig. 5 (a) shows top view of the $TM_{510}$-mode

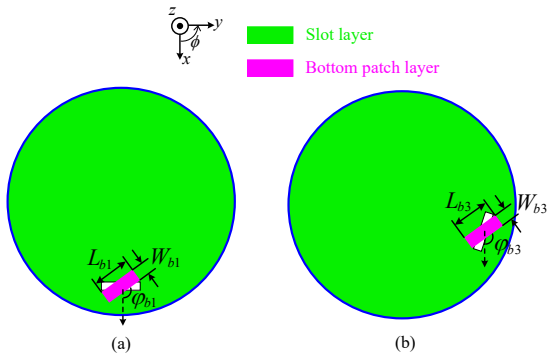


Fig. 5. Top view of the $TM_{510}$-mode patch-augmented cavity antenna without both the lower and upper substrates being presented. (a) Slot 1. (b) Slot 3.

cavity antenna augmented with a metallic rectangular patch when only Slot 1 is etched. Both the upper and lower substrates are not presented for clear observations. The metallic rectangular patch with a length of $L_{b1}$ and a width of $W_{b1}$ is printed on bottom patch layer of the upper substrate. It is orientated with an angle of $\phi_{b1}$ with respect to the $+x$-axis. All metal are removed on top patch layer of the upper substrate.

It is known that tangential E-fields radiated from the slot are aligned with $x$-axis. When the rectangular patch is closely placed above the slot with a small gap of $h_a$, the slot radiation is coupled to the patch's two long edges and, hence, antenna's tangential E-fields are converted and pointed in the direction normal to the long edges. One may infer that $\varphi_{b1}$ should be chosen as $126^\circ$ to align the far-field co-pol. E-fields along $\phi = 36^\circ$. Other parameter values (in millimeters) are: $L_s = 5.5$, $W_s = 0.7$, $R_s = 11.5$, $h_a = 0.5$, $L_{b1} = 5.5$, and $W_{b1} = 2.5$. Fig. 6 shows the simulated co-pol. and x-pol. gain patterns as well as the phase values of the co-pol. E-fields in $\phi = 126^\circ$ plane at 29.25 GHz. Note that the co-pol. gain pattern is not centered around $\theta = 0^\circ$. This is because the finite size of the slot layer produces an asymmetrical edge effect on the Slot 1's radiation. The gain value is 8.2 dBi with a x-pol. level of $-24.0$ dB at the broadside direction. It validates the successful polarization conversion that employs the closely-spaced rectangular patch. Far-field phase value is $-154.9^\circ$ at the broadside. Additional investigations show that the antenna gain patterns remain similar when the effects of the other nine slots are included.

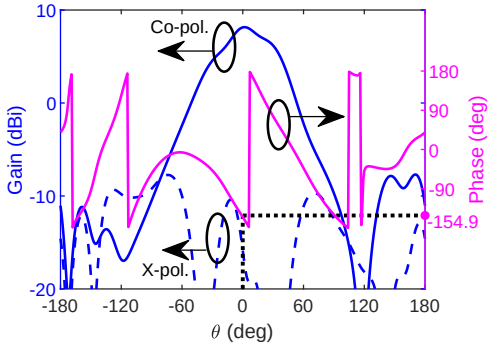


Fig. 6. Co-pol. and x-pol. gain patterns as well as the phase values of the co-pol. E-fields in $\phi = 126^\circ$ plane at 29.25 GHz.

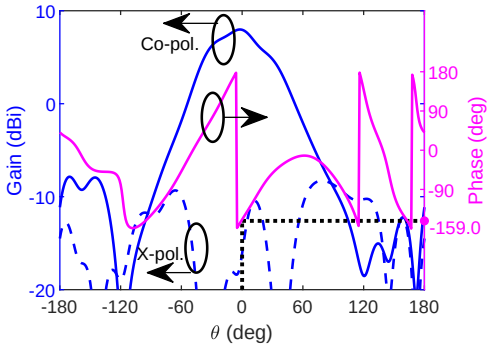


Fig. 7. Co-pol. and x-pol. gain patterns as well as the phase values of the co-pol. E-fields in $\phi = 126^\circ$ plane at 29.25 GHz.

The same method of printing a rectangular patch on the bottom patch layer is adopted to convert Slot 3's co-pol. E-fields. Fig. 5 (b) shows the top view of the $TM_{510}$-mode patch-augmented cavity antenna without both the lower and upper substrates being presented when only Slot 3 is etched. Its parameter values are optimized as: $\varphi_{b3} = 126^\circ$, $L_{b3} = 5.5$ mm, and $W_{b3} = 2.5$ mm. With the use of the augmented patch for polarization conversion, the attained far-field co-pol. is directed along $\phi = 36^\circ$. Fig. 7 shows the simulated co-pol. and x-pol. gain patterns as well as the phase values of the co-pol. E-fields in $\phi = 126^\circ$ plane at 29.25 GHz. The antenna's broadside gain value is 8.0 dBi with a x-pol. level of -24.0 dB. Far-field phase value is $-159.0^\circ$ at the broadside. Note that the far-field radiating phase values are similar for Slot 1 and 3. In the following, their phase values are set as the reference for the other slots' radiation, i.e., the reference phase value is around $-150^\circ$. The broadside phase of the E-fields radiated from each patch-augmented slot should be the same or close to this reference value. Their phase difference may decrease the gain of the final multi-LP reconfigurable antenna with all the ten patch-augmented slots present.

### *B. Study on Slot 2*

Radiating fields of Slot 2 are pointing towards the required $\phi = 36^\circ$ when only Slot 2 is etched on the slot layer. Simulations also confirm that the gain value is around 6.0 dBi with a x-pol. level of $-34.6$ dB at the broadside. Nevertheless, broadside phase value of the slot radiation is $30.5^\circ$. This value is almost out-of-phase to the reference phase value. Consequently, the patch layers printed on the upper substrate should adjust the slot's far-field radiation phase.

Fig. 8 shows the top view of the $TM_{510}$-mode cavity antenna augmented with the top and bottom patch layers when only Slot 2 is etched. Both substrates are not presented for clear observations. Right top inset illustrates a closed-up view of the top patch layer printed on top of the upper substrate. It is a rectangular patch with a length of $L_{b2}$ and a width of $W_{b2}$. The bottom patch layer is shown in right bottom inset. It is an H-shaped slotted metallic patch. The two patch layers act as phase delay element for the slot radiation. Its dimensions are denoted by $L_{b2}$, $W_{b2}$, $L_a$, $W_a$, $L_c$, and $W_c$. Both patches are centrally located to the slot center $O_2$. They are separately

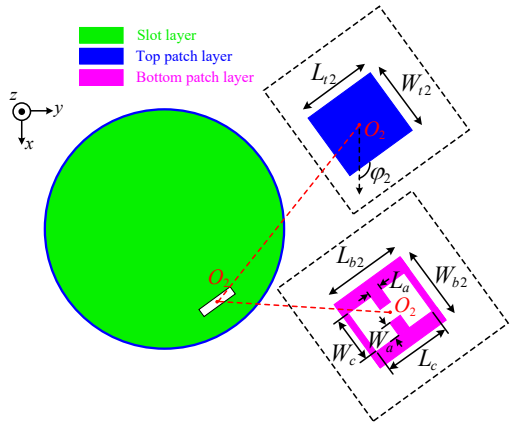


Fig. 8. Top view of the $TM_{510}$-mode cavity antenna without both the lower and upper substrates being presented when only Slot 2 is etched. Right insets present closed-up views of the metallic patch layers.

TABLE I
PARAMETER VALUES FOR THE CAVITY ANTENNA WHEN ONLY SLOT 2 IS ETCHED

| Parameter | $L_{b2}$ | $W_{b2}$ | $L_c$ | $W_c$ | $L_a$ | $W_a$ | $L_{t2}$ |
|---|---|---|---|---|---|---|---|
| Values (mm) | 5.5 | 5 | 5.25 | 3.5 | 1.1 | 1.4 | 4.25 |

drawn in right insets simply for clear observations. Their orientation angle is $\varphi_2$ = 126° with respect to +$x$-axis.

Values of the patch parameters are optimized to provide the desired phase value with an accepted gain at the broadside. A simulation model is built for this investigation. The two-layer metallic patches act as the phase delay element for the slot radiation. The near-field coupling among the slot, the H-shaped slotted patch, and the rectangular patch is crucial for the antenna's far-field gain and phase values. As an example, a parameter study was performed on the patch width $W_{t2}$. Other parameter values are fixed as shown in Table I.

Fig. 9 (a) and (b) respectively show the obtained phase and gain patterns in $\phi = 126°$ plane when $W_{t2}$ is varied. When $W_{t2}$ is chosen as 4 mm, the broadside phase value is $-50.0°$ with a gain value of 6.8 dBi. The phase and gain values, respectively, become $-98.3°$ and 7.9 dBi when $W_{t2}$ increases to 4.5 mm. This indicates the metallic patches achieve a larger phase delay and a higher broadside gain. When $W_{t2}$ further increases to 5 mm, the far-field phase value is $-66.6°$ and the gain value is only 2.75 dBi at the broadside direction. A large gain drop is observed for $W_{t2}$ = 5 mm. It is caused by the deterioration of the coupling between the slot and the metallic patches. With respect to the broadside phase and gain values, one can then conclude that the metallic patches achieve the best performance when $W_{t2}$ = 4.5 mm. Thus, $W_{t2}$ is chosen as 4.5 mm in the final design. Broadside-beam pattern is obtained with a 3-dB gain beamwidth of 88.1° in $\phi = 126°$ plane.

### C. Study on Slot 4

When only Slot 4 is etched on the slot layer, the far-field co-pol. E-fields are directed along $\phi = 108°$ at the broadside. It

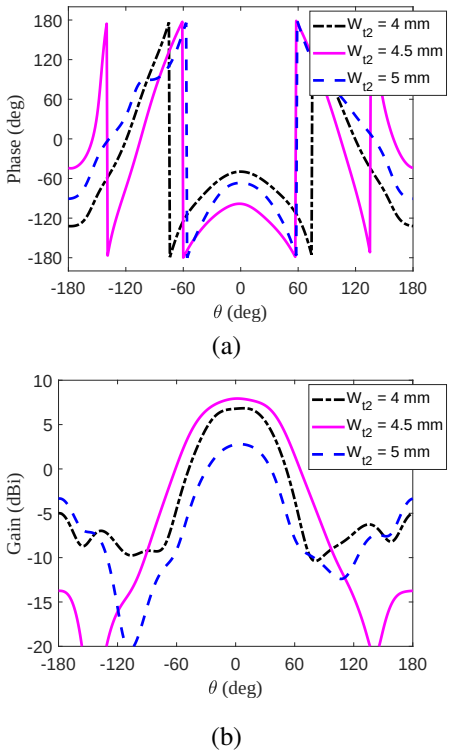


Fig. 9. Varied $W_{t2}$ for the patch-augmented $TM_{510}$-mode cavity antenna when only Slot 2 is etched. (a) The phase of the co-pol. E-fields. (b) Co-pol. gain patterns.

has a large angle (72°) difference with the desired polarization along $\phi = 36°$. One may opt to use the previous polarization conversion method of employing a single rectangular patch on the bottom patch layer. Fig. 10 (a) shows the top view of the $TM_{510}$-mode cavity antenna augmented with a single patch when only Slot 4 is etched. Both substrates are not shown for clear observations. The patch has a length of $L_4$, a width of $W_4$, and an angle of $\varphi_4$. Parameter values are optimized as: $\varphi_4$ = 126°, $L_4 = 4.5$ mm, and $W_4 = 2$ mm. It was found that the gain value and x-pol. level are only 3.3 dBi and $-3.5$ dB at the broadside, respectively. This suggests that the polarization conversion is not attainable by using this single rectangular patch.

It was then decided to introduce two rectangular patches that are respectively printed on top and bottom patch layers. Its top view without both substrates being presented is given in Fig. 10 (b). Top and bottom patch layers are centrally located with respect to the slot center $O_4$, and they are separately shown in the right insets for clear observations. The upper rectangular patch has the same dimensions with the patch in Fig. 10 (a), i.e., $\varphi_{t4}$ = 126°, $L_{t4} = 4.5$ mm, and $W_{t4} = 2$ mm. This can secure antenna's final far-field polarization being directed along $\phi = 36°$. The bottom patch has a length of $L_{b4}$, a width of $W_{b4}$, and an angle of $\varphi_{b4}$. The $L_{b4}$, $W_{b4}$, and $\varphi_{b4}$ are crucial for obtaining the desired polarization convention with acceptable phase value. Parameter study of these parameters was conducted, but it is not shown here for simplicity. Their values are eventually obtained as: $\varphi_{b4}$ = 60°, $L_{b4} = 4.5$ mm, and $W_{b4} = 2$ mm.

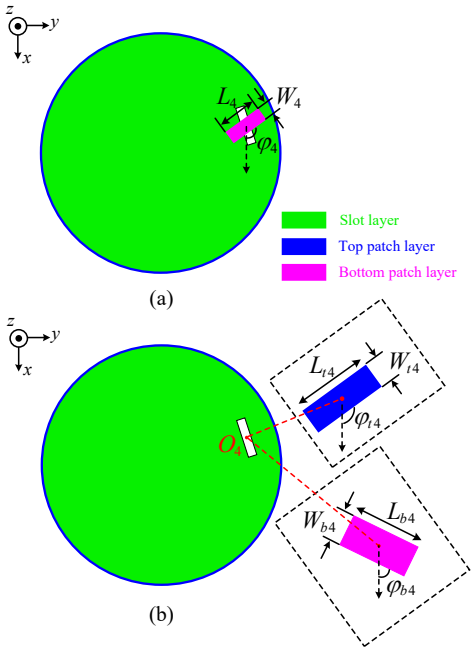


Fig. 10. Top view of the $TM_{510}$-mode cavity antenna without both the lower and upper substrates being presented when only Slot 4 is etched. (a) Single patch layer. (b) Two patch layers.

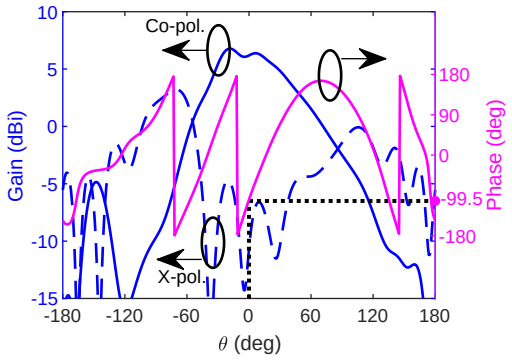


Fig. 11. Co-pol. and x-pol. gain patterns as well as the phase values of the co-pol. E-fields in $\phi = 126°$ plane at 29.25 GHz.

Fig. 11 shows the simulated co-pol. and x-pol. gain patterns as well as the phase values of the co-pol. E-fields in $\phi = 126°$ plane at 29.25 GHz. The gain value and x-pol. level are 6.2 dBi and $-16.8$ dB at the broadside, respectively. The broadside radiating phase value is $-99.5°$.

### *D. Study on Slot 5*

A similar large polarization angle difference occurs between the Slot 5's polarization along $\phi = 144°$ and the reference $\phi = 36°$. Following the above process of polarization conversion for Slot 4, two patch layers are also implemented and printed on top and bottom of the upper substrate, respectively. Fig. 12 shows top view of the $TM_{510}$-mode cavity antenna augmented with two patch layers when only Slot 5 is etched. Top and bottom patch layers are centrally located with respect to the slot center $O_5$, and they are separately shown in the right insets. Parameter values of the two patches are: $\varphi_{t5}$ = 126°,

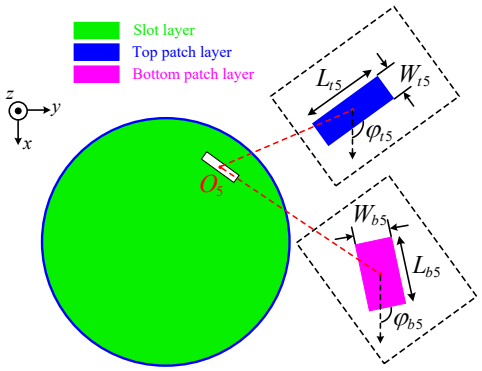


Fig. 12. Top view of the $TM_{510}$-mode cavity antenna augmented with two patch layers when only Slot 5 is etched. Both the lower and upper substrates are not shown for clear observations.

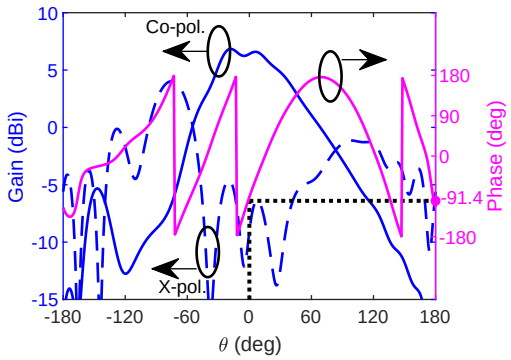


Fig. 13. Co-pol. and x-pol. gain patterns as well as the phase values of the co-pol. E-fields in $\phi = 126°$ plane at 29.25 GHz when only Slot 5 is etched.

$L_{t5} = 4.5$ mm, and $W_{t5} = 2.25$ mm, $\varphi_{b5}$ = 100°, $L_{b5} = 4.5$ mm, and $W_{b5} = 2.25$ mm. Fig. 13 shows the obtained co-pol. and x-pol. gain patterns as well as the phase values of the co-pol. E-fields in $\phi = 126°$ plane at 29.25 GHz. The gain value and x-pol. level are 6.4 dBi and $-15.4$ dB at the broadside, respectively. The broadside radiating phase value is $-91.4°$.

## IV. Basic Multi-LP Reconfigurable Antenna

In the five single-slot cavity antenna models, appropriate patches are introduced and printed on the upper substrate to align each slot's polarization along $\phi$ = 36° with close phase values. To form the high-gain broadside beam with a low x-pol. level for the cavity antenna etched with an array of ten slots, one may straightforwardly accumulate all of the corresponding patches employed in the separate analysis for each slot's radiation. Fig. 14 (a) and (b), respectively, show the accumulated bottom and top patch layers printed on the upper substrate. The radius $R_s$ of the substrate is 25 mm. A circular array of through-holes at an interval of 36° is drilled to facilitate the alignment and assembly of the whole antenna. Fig. 15 depicts the side view of the basic multi-LP reconfigurable antenna. The patches' dimensions have the same values as those obtained in the initial studies. On bottom plane of the cavity, stepped slots are etched for impedance

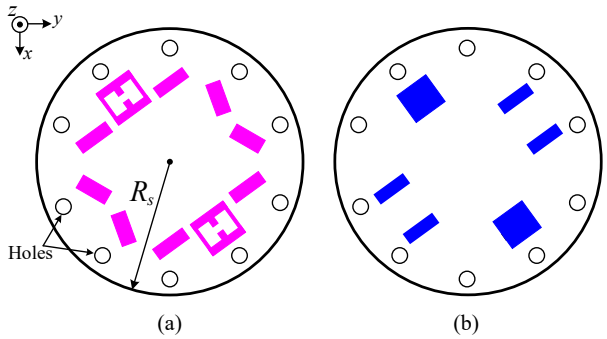


Fig. 14. Top view of the accumulated bottom and top patch layers printed on the upper substrate (State A). (a) Bottom patch layer. (b) Top patch layer.

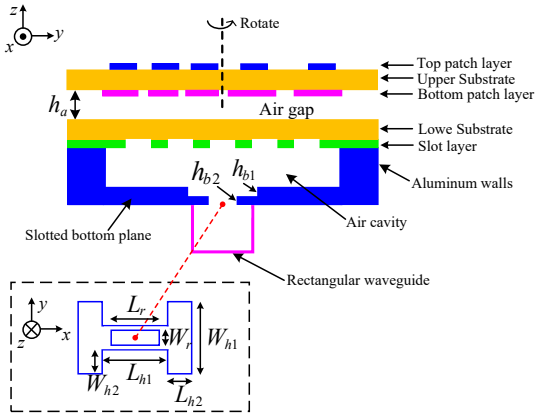


Fig. 15. Side view of the basic multi-LP reconfigurable antenna. Top view of the stepped slots are shown in the bottom inset.

transition from the rectangular waveguide to the resonant air-cavity antenna. Top view of the stepped slots is shown in bottom inset of Fig. 15. It is an H-shaped slot with a depth of $h_{b1}$ = 1.5 mm followed by a rectangular slot with a depth of $h_{b2}$ = 1 mm. Dimensions (in millimeters) of the H-shaped slot are given by: $L_{h1}$ = 6, $L_{h2}$ = 2.5, $W_{h1}$ = 6.75, and $W_{h2}$ = 2. The rectangular slot has a length of $L_r$ = 5 mm and a width of $W_r$ = 1.25 mm. The slot layer remains the same as the one shown in Fig. 4.

When the upper substrate printed with the top and bottom patch layers is non-rotated as shown in Fig. 14, the antenna should radiate a broadside beam and have a LP state along $\phi = 36°$. This initial state is labeled as State A. After the upper substrate is rotated with its rotation angle ranging from 36° to 144° at an interval of 36°, other four LP states, i.e., $\phi$ = [72°, 108°, 144°, 180°], can be realized, and they are sequentially marked as State B to E. Fig. 16 shows the simulated S-parameters for the five switchable LP states. Simulated overlapped $|S_{11}| \leq -10$ dB bandwidth ranges from 28.99 to 29.48 GHz (490 MHz). This narrow bandwidth is associated with the higher-order $TM_{510}$-mode cavity. It is known that the bandwidth of a resonant cavity increases as the mode order decreases. One can improve the bandwidth by using a lower-order cavity and, subsequently, the number of the obtained LPs and peak realized gain values will be reduced. On the other hand, if the objective is to increase the

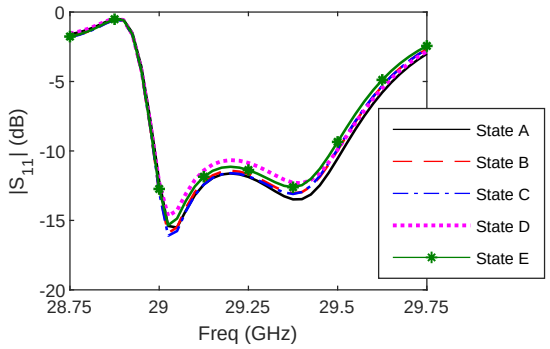


Fig. 16. Simulated S-parameters for the basic multi-LP reconfigurable antenna.

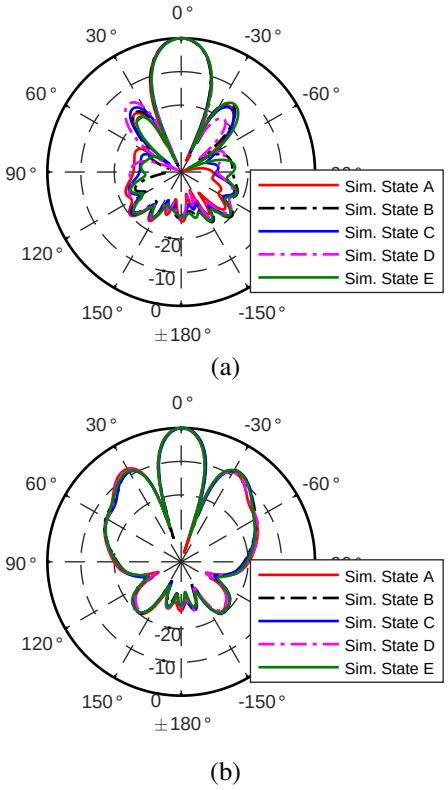


Fig. 17. Simulated co-pol. radiation patterns for the five LP states when the source frequency is 29.25 GHz. (a) E plane. (b) H plane.

number of the LPs, one can even increase the mode order, albeit reducing the bandwidth further. In short, the presented research provides a new way of achieving multi-LPs with low complexity and low loss.

Fig. 17 shows the simulated E- and H-plane co-pol. radiation patterns for the five LP states when the source frequency is 29.25 GHz. It is observed that the radiation patterns are almost invariant for all of these five LP states. The 3-dB beamwidth is 20.5° in E-plane, and it is 15.9° in H-plane. The sidelobe level is around −14.4 and −7.5 dB in E and H plane, respectively. Fig. 18 shows the simulated co-pol. and x-pol. realized gains for the five LP states. The overlapped 3-dB gain bandwidth ranges from 28.95 to 29.73 GHz (780 MHz). At the operating band from 28.99 to 29.48 GHz, the overlapped realized gains

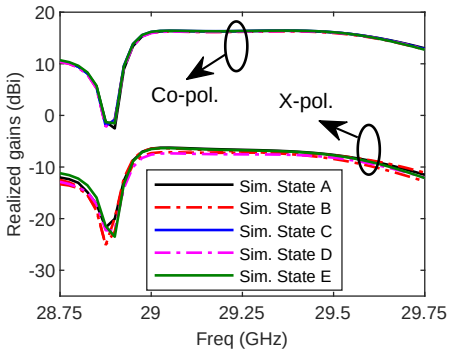


Fig. 18. Simulated co-pol. and x-pol. realized gains for the five LP states.

are varied between 16.1 and 16.4 dBi. The x-pol. levels are lower than −23 dB for all the five LP states.

## V. Optimized Multi-LP Reconfigurable Antenna

A high sidelobe level of −7.5 dB was noticed in the radiation patterns at 29.25 GHz for all the five LP states. For each LP operating state, the far-field radiation is mainly contributed by the circular array of the ten patch-augmented slots. The value −7.5 dB is close to the theoretical sidelobe value (−7.9 dB) of the ten-element uniform circular array excited with equal amplitudes and phases [31]. One method to reduce the sidelobe level is locating additional in-phase radiating elements inside the circular array.

### A. Antenna Configuration and Performance

A simple yet effective method is presented that employs a modified bottom patch layer for the multi-LP antenna to suppress its sidelobe level. This multi-LP antenna with a modified bottom patch layer is named as the optimized multi-LP reconfigurable antenna. Fig. 19 shows the configuration of the modified bottom patch layer. It is obtained by incorporating four additional patches with eight connecting strips into the previous bottom patch layer. All of the additional patches have a length of $L_{a1}$ and a width of $W_{a1}$. They are oriented with an angle of $\phi_a$ = 126° with respect to +$x$-axis. Each additional

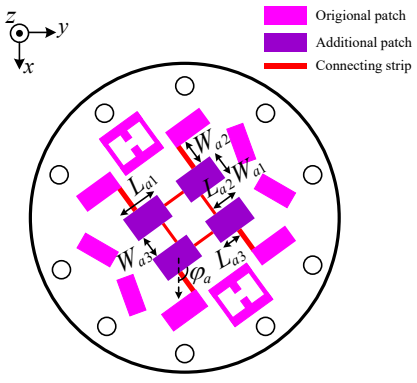


(a)

Fig. 19. Configuration of the modified bottom patch layer (State A).

TABLE II
Parameter Values for the Modified Bottom Patch Layer

| Parameter | $L_{a1}$ | $W_{a1}$ | $L_{a2}$ | $W_{a2}$ | $L_{a3}$ | $W_{a3}$ |
|---|---|---|---|---|---|---|
| Values (mm) | 6.5 | 4 | 3.75 | 2.55 | 2.5 | 3 |

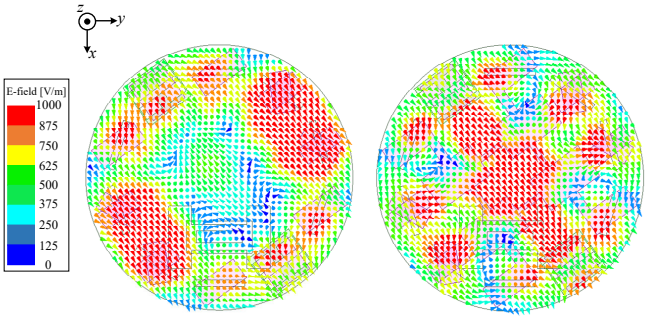


(a) (b)

Fig. 20. Top view of the E-fields distribution (State A) above the $TM_{510}$-mode patch-augmented cavity. (a) The basic multi-LP antenna. (b) The optimized multi-LP antenna.

patch is connected to a corresponding original patch through a thin strip. These additional patches are also connected to each other using metallic strips. Dimensions of these strips are denoted by: $L_{a2}$, $L_{a3}$, $W_{a2}$, and $W_{a3}$. Values (in millimeters) for the parameters are optimized and given in Table II.

Fig. 20 (a) and (b) show the top view of the E-fields above the $TM_{510}$-mode patch-augmented cavity as a snapshot for the basic and optimized multi-LP antennas, respectively. It is observed that the E-fields for the basic multi-LP antenna are mainly distributed around the circular array of the ten patch-augmented slots. Small values of the E-fields are observed inside the circle as there is no radiating element. When the

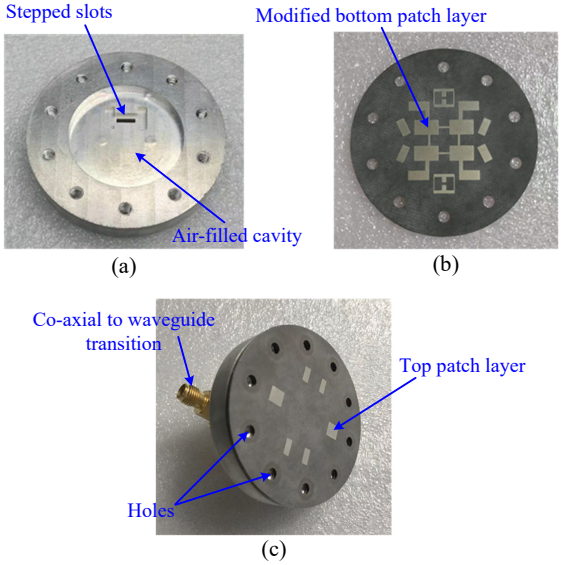


Fig. 21. Fabricated antenna prototype before and after assembly. (a) Air-filled cavity. (b) Modified bottom patch layer. (c) Side view of the assembled antenna.

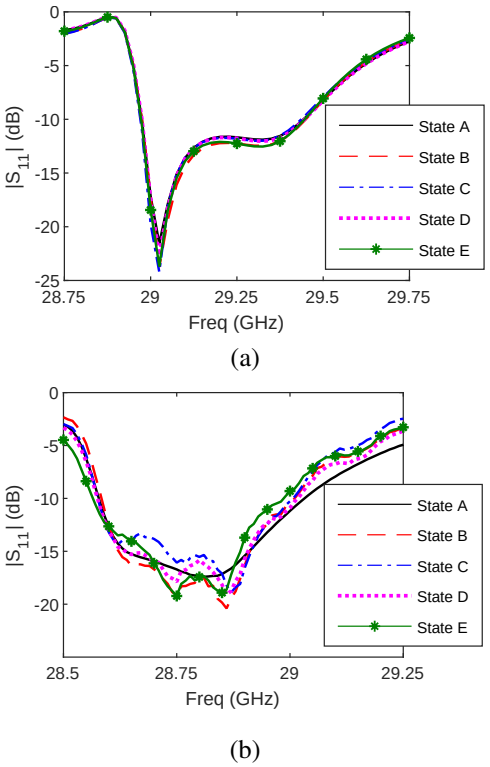


Fig. 22. S-parameters of the optimized multiple-LP reconfigurable antenna. (a) Simulated $|S_{11}|$. (b) Measured $|S_{11}|$.

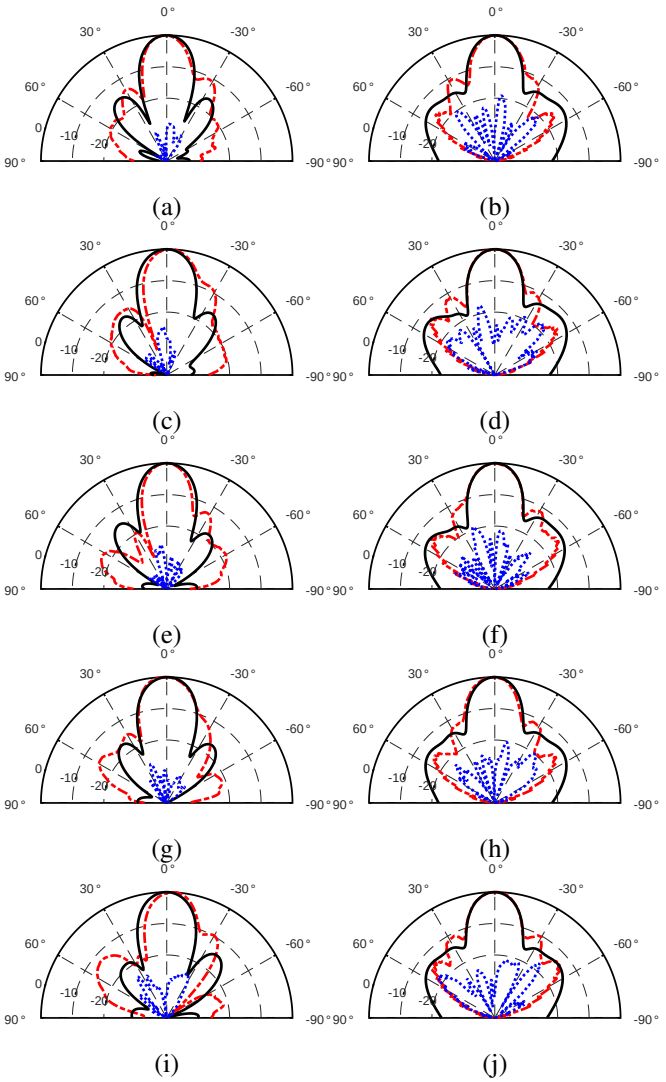


Fig. 23. Measured (simulated) radiation patterns of the optimized multi-LP antenna when the source frequency is 28.8 GHz (29.25 GHz). Red dash-dot line: measured co-pol.. Blue dot line: measured x-pol.. Black solid line: simulated co-pol.. (a) E plane at State A. (b) H plane at State A. (c) E plane at State B. (d) H plane at State B. (e) E plane at State C. (f) H plane at State C. (g) E plane at State D. (h) H plane at State D. (i) E plane at State E. (j) H plane at State E.

additional patches and connecting strip are incorporated into the bottom patch layer of the optimized multi-LP antenna, strong in-phase resonant E-fields are produced among these patches and strips. This is equivalent to introducing additional in-phase radiating elements inside the circular slot array and, hence, the obtained sidelobe level can be reduced [32]. Moreover, these additional in-phase radiating elements also increase the antenna gain.

The final optimized multi-LP antenna was constructed and simulated. A prototype was fabricated and assembled as shown in Fig. 21. As a proof of concept, the rotation of the upper substrate is implemented in a manual way in the measurement. In practice, a stepper motor can be placed behind the slot-based cavity of the multi-LP antenna. The upper substrate is connected to the motor platform through supporting posts. One can then accomplish the rotation of the substrate by controlling the motor. Fig. 22 (a) and (b), respectively, show the simulated and measured S-parameters for all the five LP states. The simulated overlapped $|S_{11}| \leq -10$ dB bandwidth is ranging from 28.97 to 29.44 GHz (470 MHz) while the measured one is red shifted to lower frequencies, from 28.58 to 28.99 GHz (410 MHz). This frequency shift is likely caused by the inaccuracies of the cavity radius $R_c$ and the surface irregularity of the substrates existed in the fabricated prototype. The $R_c$ is a critical parameter that determines the antenna's operating band. One can use special fabrication techniques, such as the electric spark discharge machining and the low-speed wire-cut electrical discharge machining, to improve the accuracy of the $R_c$. The substrate surface irregularity will affect the air gap $h_a$ between the lower and upper substrates, which is another critical parameter for impedance matching. One may utilize high end or thicker substrates in the design to avoid this problem. With such bandwidth, the antenna proposed can be used in certain 5G mm-wave applications. With further development, the technology is expected to be able to serve 5G mm-wave systems in general.

Fig. 23 shows the measured (simulated) E-plane and H-plane co-pol. radiation patterns for the five LP states of the optimized multi-LP antenna at 28.8 GHz (29.25 GHz). The simulated sidelobe levels are lower than $-13$ dB in both E- and H-planes for all the five LP states. The measured sidelobe levels are around $-10$ dB. Some discrepancies were observed between the simulated and measured radiation patterns, especially for the E-field patterns. Our simulation results suggest that this is caused by the inaccuracies of the cavity radius

TABLE III
DETAILED COMPARISON BETWEEN THE ANTENNA DEVELOPED IN THIS WORK AND THOSE REPORTED PREVIOUSLY

| Reference antenna | Operating band (GHz) | Aperture size ($\lambda_0^2$) | Realized gain (dBi) | Radiation efficiency (%) | LPs number | Reconfiguration technique |
|---|---|---|---|---|---|---|
| [21] | 2.33 – 2.5 | 0.32 | 5.3 – 5.9 | 82.9 – 84.7* | 4 | PIN diode |
| [22] | (∼)1.97 – 2.02 | 0.44 | 6.7 – 6.9 | 79 | 4 | PIN diode |
| [23] | 2.2 – 3.1 | 0.61 | 5.0 – 5.2 | (∼) 70.0 – 90.0 | 4 | PIN diode |
| [24] | 2.3 – 4.0 | 0.84 | 6.8 – 10.9 | (∼) 70.0 – 86.0 | 4 | PIN diode |
| [25] | 2.85 – 3.40 | 1.41 | (∼) 4.0 – 8.3 | 65.1 – 74.4 | 5 | PIN diode |
| This work | 28.58 – 28.99 | 6.08 | 15.5 – 16.8 | 97.8 – 99.6* | 5 | Mechanical rotation |

*represents the simulation results; (∼) indicates the data obtained through virtual measurement.

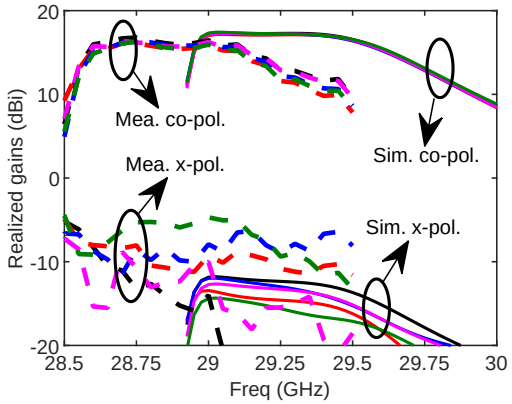


Fig. 24. Simulated and measured co-pol. and x-pol. realized gains of the optimized multi-LP antenna for its five reconfigurable LP states.

$R_c$ and the surface irregularity in the fabricated prototype. Fig. 24 shows the simulated and measured realized gains of the optimized multi-LP antenna for its five reconfigurable LP states. The simulated/measured gains remain similar for all the five LPs. The simulated overlapped 3-dB gain bandwidth ranges from 28.94 to 29.68 GHz, and the peak realized gain is 17.4 dBi at 29.05 GHz. As previously noted, the measured results show a red shift to lower frequencies. The measured overlapped 3-dB gain bandwidth ranges from 28.57 to 29.22 GHz, and the peak value is 16.8 dBi at 28.75 GHz. The measured x-pol. levels are lower than $-20$ dB.

### B. Discussion

A detailed comparison between our developed antenna and those previously reported multi-LP antennas is provided in Table III. All of those reported multi-LP antennas in [21]–[25] are operating at low frequencies, i.e., less than 5 GHz. In contrast, the developed antenna operates in the mm-wave band. One finds that a wide operating bandwidth is achieved for the antennas in [23]–[25]. Nevertheless, only the one in [25] can realize more than 4 LPs. It employs a number of dipole radiators controlled by the PIN diodes, but only a single dipole radiator is working for any given LP state, which limits the peak gain of the antenna. The attained realized gain ranges from 4 to 8.3 dBi. If one desires a higher gain, an antenna array can be used while a large number of PIN diodes are required with more insertion losses. On the other hand, our antenna behaves as a ten-element circular array, and the obtained realized gains are high, ranging from 15.5 to 16.8 dBi. Furthermore, the mechanical reconfiguration avoids large losses in the PIN diodes. The cost is a narrower bandwidth and a lower switching speed.

## VI. CONCLUSION

A mm-wave cavity-backed multi-LP antenna was developed that can achieve five switchable LP states by rotating its upper substrate with a 36° interval. The upper substrate was "excited" by the base slotted $TM_{510}$-mode cavity, which has a rotationally-symmetrical property. The multi-LP reconfiguration with rotating upper substrate was then simplified to achieve a high-gain LP beam with low x-pol. level when the upper substrate is initially fixed. To reach this goal, each slot radiation was separately monitored and investigated by using single-slot cavity antenna models. The patch surfaces printed on the upper substrate were properly engineered for each slot's radiation adjustment. The realized multi-LP antenna obtains similar radiation patterns and stable realized gains for the five LP states. Unsurprisingly, a high sidelobe level was produced by composite radiation of the circular array of ten patch-augmented slots. A simple method that modifies the bottom patch layer was utilized to optimize the antenna's radiation performance. For the five LP states of the optimized multi-LP antenna, the realized gains are varied from 15.5 to 16.8 dBi. Simulated and measured sidelobe levels are around $-13$ and $-10$ dB, respectively. The developed mm-wave cavity-backed multi-LP antenna serves as a good candidate for 5G and beyond wireless systems.

## REFERENCES

[1] C. G. Christodoulou, Y. Tawk, S. A. Lane, and S. R. Erwin, "Reconfigurable antennas for wireless and space applications," *Proc. IEEE*, vol. 100, no. 7, pp. 2250–2261, 2012.
[2] P. Qin, F. Wei, and Y. J. Guo, "A wideband-to-narrowband tunable antenna using a reconfigurable filter," *IEEE Trans. Antennas Propag.*, vol. 63, no. 5, pp. 2282–2285, 2015.
[3] J. G. Nicholls and S. V. Hum, "Full-space electronic beam-steering transmitarray with integrated leaky-wave feed," *IEEE Trans. Antennas Propag.*, vol. 64, no. 8, pp. 3410–3422, 2016.
[4] C. Borda-Fortuny, K.-F. Tong, A. Al-Armaghany, and K.-K. Wong, "A low-cost fluid switch for frequency-reconfigurable vivaldi antenna," *IEEE Antennas Wireless Propag. Lett.*, vol. 16, pp. 3151–3154, 2017.
[5] Z. Ren, S. Qi, Z. Hu, Z. Shen, and W. Wu, "Wideband water helical antenna of circular polarization," *IEEE Trans. Antennas Propag.*, vol. 67, no. 11, pp. 6770–6777, 2019.

[6] E. Abdo-Sanchez, A. Epstein, and G. V. Eleftheriades, "Reconfigurability mechanisms with scanning rate control for omega-bianisotropic huygens' metasurface leaky-wave antennas," *IEEE Access*, vol. 7, pp. 168 247–168 260, 2019.
[7] J. Park, M. Choo, S. Jung, D. Choi, J. Choi, and W. Hong, "A software-programmable directivity, beamsteering, and polarization reconfigurable block cell antenna concept for millimeter-wave 5G phased- array architectures," *IEEE Trans. Antennas Propag.*, vol. 69, no. 1, pp. 146–154, 2021.
[8] F. Wu and K. M. Luk, "A reconfigurable magneto-electric dipole antenna using bent cross-dipole feed for polarization diversity," *IEEE Antennas Wireless Propag. Lett.*, vol. 16, pp. 412–415, 2017.
[9] Y. Cui, C. Qi, and R. Li, "A low-profile broadband quad-polarization reconfigurable omnidirectional antenna," *IEEE Trans. Antennas Propag.*, vol. 67, no. 6, pp. 4178–4183, 2019.
[10] J.-S. Row and Y.-H. Wei, "Wideband reconfigurable crossed-dipole antenna with quad-polarization diversity," *IEEE Trans. Antennas Propag.*, vol. 66, no. 4, pp. 2090–2094, 2018.
[11] N. Nguyen-Trong, S. X. Ta, M. Ikram, K. Bertling, and A. M. Abbosh, "A low-profile wideband tripolarized antenna," *IEEE Trans. Antennas Propag.*, vol. 67, no. 3, pp. 1946–1951, 2019.
[12] L. Zhang *et al.*, "A quad-polarization reconfigurable antenna with suppressed cross polarization based on characteristic mode theory," *IEEE Trans. Antennas Propag.*, pp. 1–1, 2020.
[13] M. Li, Z. Zhang, and M. C. Tang, "A compact, low-profile, wideband, electrically controlled, tri-polarization-reconfigurable antenna with quadruple gap-coupled patches," *IEEE Trans. Antennas Propag.*, vol. 68, no. 8, pp. 6395–6400, 2020.
[14] W. Lin and H. Wong, "Wideband circular polarization reconfigurable antenna," *IEEE Trans. Antennas Propag.*, vol. 63, no. 12, pp. 5938–5944, 2015.
[15] ——, "Wideband circular-polarization reconfigurable antenna with L-shaped feeding probes," *IEEE Antennas Wireless Propag. Lett.*, vol. 16, pp. 2114–2117, 2017.
[16] L. Zhang, S. Gao, Q. Luo, P. R. Young, and Q. Li, "Wideband loop antenna with electronically switchable circular polarization," *IEEE Antennas Wireless Propag. Lett.*, vol. 16, pp. 242–245, 2017.
[17] A. Khidre, K. Lee, F. Yang, and A. Z. Elsherbeni, "Circular polarization reconfigurable wideband e-shaped patch antenna for wireless applications," *IEEE Trans. Antennas Propag.*, vol. 61, no. 2, pp. 960–964, 2013.
[18] H. L. Zhu, S. W. Cheung, X. H. Liu, and T. I. Yuk, "Design of polarization reconfigurable antenna using metasurface," *IEEE Trans. Antennas Propag.*, vol. 62, no. 6, pp. 2891–2898, 2014.
[19] L. Ji, P. Qin, Y. J. Guo, C. Ding, G. Fu, and S. Gong, "A wideband polarization reconfigurable antenna with partially reflective surface," *IEEE Trans. Antennas Propag.*, vol. 64, no. 10, pp. 4534–4538, 2016.
[20] A. Bhattacharjee, S. Dwari, and M. K. Mandal, "Polarization-reconfigurable compact monopole antenna with wide effective bandwidth," *IEEE Antennas Wireless Propag. Lett.*, vol. 18, no. 5, pp. 1041–1045, 2019.
[21] S.-L. Chen, F. Wei, P.-Y. Qin, Y. J. Guo, and X. Chen, "A multi-linear polarization reconfigurable unidirectional patch antenna," *IEEE Trans. Antennas Propag.*, vol. 65, no. 8, pp. 4299–4304, 2017.
[22] H. Gu, J. Wang, L. Ge, and C. Sim, "A new quadri-polarization reconfigurable circular patch antenna," *IEEE Access*, vol. 4, pp. 4646–4651, 2016.
[23] H. Wong, W. Lin, L. Huitema, and E. Arnaud, "Multi-polarization reconfigurable antenna for wireless biomedical system," *IEEE Trans. Biomed. Circuits Syst.*, vol. 11, no. 3, pp. 652–660, 2017.
[24] H. H. Tran, N. Nguyen-Trong, T. T. Le, A. M. Abbosh, and H. C. Park, "Low-profile wideband high-gain reconfigurable antenna with quad-polarization diversity," *IEEE Trans. Antennas Propag.*, vol. 66, no. 7, pp. 3741–3746, 2018.
[25] D. Chen, Y. Liu, S. L. Chen, P. Y. Qin, and Y. J. Guo, "A wideband high-gain multi-linear polarization reconfigurable antenna," *IEEE Trans. Antennas Propag.*, pp. 1–1, 2020.
[26] W. Hong, K. Baek, Y. Lee, Y. Kim, and S. Ko, "Study and prototyping of practically large-scale mmwave antenna systems for 5G cellular devices," *IEEE Commun. Mag.*, vol. 52, no. 9, pp. 63–69, 2014.
[27] L. Chang, Z. Zhang, Y. Li, S. Wang, and Z. Feng, "Air-filled long slot leaky-wave antenna based on folded half-mode waveguide using silicon bulk micromachining technology for millimeter-wave band," *IEEE Trans. Antennas Propag.*, vol. 65, no. 7, pp. 3409–3418, 2017.
[28] O. Zetterstrom, E. Pucci, P. Padilla, L. Wang, and O. Quevedo-Teruel, "Low-dispersive leaky-wave antennas for mmWave point-to-point high-throughput communications," *IEEE Trans. Antennas Propag.*, vol. 68, no. 3, pp. 1322–1331, 2020.
[29] E. Al Abbas, N. Nguyen-Trong, A. T. Mobashsher, and A. M. Abbosh, "Polarization-reconfigurable antenna array for millimeter-wave 5G," *IEEE Access*, vol. 7, pp. 131 214–131 220, 2019.
[30] P. Mei, S. Zhang, and G. F. Pedersen, "A wideband 3-D printed reflectarray antenna with mechanically reconfigurable polarization," *IEEE Antennas Wireless Propag. Lett.*, vol. 19, no. 10, pp. 1798–1802, 2020.
[31] H. L. Van Trees, *Optimum array processing: Part IV of detection, estimation, and modulation theory*. New York, USA: John Wiley & Sons, 2004.
[32] M. T. Ma, *Theory and Application of Antenna Arrays*. Hoboken, NJ, USA: Wiley, 1974.

**Shu-Lin Chen** (M'20) was born in Hubei Province, China. He received the B.S. degree in electrical engineering from Fuzhou University (FZU), China, in 2012; the M.S. degree in electromagnetic field and microwave technology from Xiamen University (XMU), China, in 2015; and the Ph.D. degree in engineering from the University of Technology Sydney (UTS), Australia, in 2019.

From April to July 2019, he was a Visiting Scholar with the State Key Laboratory of Terahertz and Millimeter Waves, City University of Hong Kong (CityU). Since September 2019, he has been a post-doctoral research associate with the Global Big Data Technologies Centre (GBDTC), UTS, Australia. His research interests include reconfigurable antennas, leaky-wave antennas, and millimeter-wave antennas. He was a finalist of ISAP 2017 best paper competition, and his paper was listed as an Honorary Mention in APS-URSI 2017.

**Yanhui Liu** (M'2015-SM'2019) received the B.S. and Ph.D. degrees both in electrical engineering from the University of Electronic Science and Technology of China (UESTC) in 2004 and 2009, respectively.

From September 2007 to June 2009, he was a Visiting Scholar in the Department of Electrical Engineering at Duke University, Durham, NC. In July 2011, he joined in the Department of Electronic Science, Xiamen University, China, where he was lately promoted as a Full Professor. From September to December in 2017, he was a Visiting Professor at State Key Laboratory of Millimeter Waves in City University of Hong Kong. From December 2017 to December 2019, he had been with Global Big Data Technologies Centre, University of Technology Sydney (UTS) as a Visiting Professor/Research Principal. From November 2019, he has been a Professor at UESTC. He received the UESTC Outstanding Graduate Award in 2004, and the Excellent Doctoral Dissertation Award of Sichuan Province of China in 2011. He has authored and co-authored over 160 peer-reviewed journal and conference papers including 95 SCI-indexed papers. He holds 21 Chinese invention patents in antennas and applied electromagnetics.

Dr. Liu is serving as a reviewer for a dozen of SCI-indexed journals. Since 2018, he has served as an Associate Editor for the IEEE Access. He has served many times as TPC member/reviewer/session chair in a number of international conferences in the field of antennas and propagation. His research interests include antenna array design, reconfigurable antennas, and electromagnetic scattering and imaging.

**He Zhu** (M'18) received the Bachelor and Master degree from South China University of Technology, Guangzhou, China, in 2011 and 2014, respectively, and the Ph.D. degree in Electrical Engineering from the School of ITEE, University of Queensland, Brisbane, Australia, in 2017. He is currently a Postdoctoral Research Fellow with Global Big Data Technologies Centre (GBDTC), University of Technology Sydney (UTS), Ultimo, NSW, Australia.

His research interests include development of passive and tunable microwave and mm-wave devices, radio frequency integrated circuits and systems, and beam-forming networks for antenna arrays.

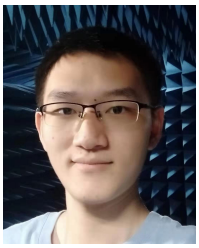

**Dingzhao Chen** was born in Changsha, China. He received the B.S. degree in electronic information science and technology from Xiamen University, Xiamen, China, in 2018, where he is currently pursuing the Ph.D. degree with the Institute of Electromagnetics and Acoustics. His current research interests include reconfigurable antennas and antenna arrays.

**Y. Jay Guo** (Fellow'2014) received a Bachelor Degree and a Master Degree from Xidian University in 1982 and 1984, respectively, and a PhD Degree from Xian Jiaotong University in 1987, all in China. His research interest includes antennas, mm-wave and THz communications and sensing systems as well as big data technologies. He has published four books and over 600 research papers including over 280 IEEE Transactions papers, and he holds 26 patents. He is a Fellow of the Australian Academy of Engineering and Technology, a Fellow of IEEE and a Fellow of IET, and was a member of the College of Experts of Australian Research Council (ARC, 2016-2018). He has won a number of most prestigious Australian Engineering Excellence Awards (2007, 2012) and CSIRO Chairman's Medal (2007, 2012). He was named one of the most influential engineers in Australia in 2014 and 2015, respectively, and one of the top researchers across fields in Australia in 2020.

He is a Distinguished Professor and the Director of Global Big Data Technologies Centre (GBDTC) at the University of Technology Sydney (UTS), Australia. Prior to this appointment in 2014, he served as a Director in CSIRO for over nine years. Before joining CSIRO, he held various senior technology leadership positions in Fujitsu, Siemens and NEC in the U.K.

Prof Guo has chaired numerous international conferences and served as guest editors for a number of IEEE publications. He is the Chair of International Steering Committee, International Symposium on Antennas and Propagation (ISAP). He has been the International Advisory Committee Chair of IEEE VTC2017, General Chair of ISAP2022, ISAP2015, iWAT2014 and WPMC'2014, and TPC Chair of 2010 IEEE WCNC, and 2012 and 2007 IEEE ISCIT. He served as Guest Editor of special issues on "*Low-Cost Wide-Angle Beam Scanning Antennas*", "*Antennas for Satellite Communications*" and "*Antennas and Propagation Aspects of 60-90 GHz Wireless Communications*," all in IEEE Transactions on Antennas and Propagation, Special Issue on "*Communications Challenges and Dynamics for Unmanned Autonomous Vehicles*," IEEE Journal on Selected Areas in Communications (JSAC), and Special Issue on ''*5G for Mission Critical Machine Communications*", IEEE Network Magazine.